

The CHESSE survey of the L1157-B1 bow-shock: high and low excitation water vapor [★]

G. Busquet¹, B. Lefloch^{2,3}, M. Benedettini¹, C. Ceccarelli², C. Codella⁴, S. Cabrit⁵, B. Nisini⁶, S. Viti⁷, A. I. Gómez-Ruiz⁴, A. Gusdorf⁸, A. M. di Giorgio¹, and L. Wiesenfeld²

¹ INAF - Istituto di Astrofisica e Planetologia Spaziali, Via del Fosso del Cavaliere 100, I-00133 Roma, Italy

² UJF-Grenoble 1 / CNRS-INSU, Institut de Planétologie et d'Astrophysique de Grenoble (IPAG) UMR 5274, Grenoble F-38041, France

³ Centro de Astrobiología, CSIC-INTA, Carretera de Torrejón a Ajalvir, km 4, Torrejón de Ardoz, E-28850 Madrid, Spain

⁴ INAF, Osservatorio Astrofisico di Arcetri, Largo Enrico Fermi 5, I-50125 Firenze, Italy

⁵ Observatoire de Paris, LERMA, UMR 8112 du CNRS, ENS, UPMC, UCP, 61 Av. de l'Observatoire, F-75014 Paris, France

⁶ INAF-Osservatorio Astronomico di Roma, Via di Frascati 33, I-00040 Monte Porzio Catone, Italy

⁷ Department of Physics and Astronomy, University College London, Gower Street, London, WC1E 6BT, UK

⁸ LERMA, UMR 8112 du CNRS, Observatoire de Paris, École Normale Supérieure, 24 rue Lhomond, 75231 Paris Cedex 05, France

Received / Accepted

ABSTRACT

Context. Molecular outflows powered by young protostars strongly affect the kinematics and chemistry of the natal molecular cloud through strong shocks resulting in substantial modifications of the abundance of several species. In particular, water is a powerful tracer of shocked material due its sensitivity to both physical conditions and chemical processes.

Aims. As part of the “Chemical Herschel Surveys of Star forming regions” (CHESSE) guaranteed time key program, we aim at investigating the physical and chemical conditions of H₂O in the brightest shock region B1 of the L1157 molecular outflow.

Methods. We observed several ortho- and para-H₂O transitions using HIFI and PACS instruments on board *Herschel* toward L1157-B1, providing a detailed picture of the kinematics and spatial distribution of the gas. We performed a Large Velocity Gradient (LVG) analysis to derive the physical conditions of H₂O shocked material, and ultimately obtain its abundance.

Results. We detected 13 H₂O lines with both instruments probing a wide range of excitation conditions. This is the largest data set of water lines observed in a protostellar shock that provide both the kinematics and the spatial information of the emitting gas. PACS maps reveal that H₂O traces weak and extended emission associated with the outflow identified also with HIFI in the o-H₂O line at 556.9 GHz, and a compact (~10'') bright, higher-excitation region. The LVG analysis of H₂O lines in the bow-shock show the presence of two gas components with different excitation conditions: a warm ($T_{\text{kin}} \approx 200\text{-}300$ K) and dense ($n(\text{H}_2) \approx (1\text{-}3) \times 10^6 \text{ cm}^{-3}$) component with an assumed extent of 10'' and a compact (~2''-5'') and hot, tenuous ($T_{\text{kin}} \approx 900\text{-}1400$ K, $n(\text{H}_2) \approx 10^{3\text{-}4} \text{ cm}^{-3}$) gas component, which is needed to account for the line fluxes of high E_u transitions. The fractional abundance of the warm and hot H₂O gas components is estimated to be $(0.7\text{-}2) \times 10^{-6}$ and $(1\text{-}3) \times 10^{-4}$, respectively. Finally, we identified an additional component in absorption in the HIFI spectra of H₂O lines connecting with the ground state level. This absorption probably arises from the photodesorption of icy mantles of a water-enriched layer at the edges of the cloud, driven by the external UV illumination of the interstellar radiation field.

Key words. stars: formation – ISM: individual objects: L1157-B1 –ISM: molecules –ISM: abundances –ISM: jets and outflows

1. Introduction

Molecular outflows are among the most conspicuous manifestation of a nascent star. These outflows are known to result from the entrainment of circumstellar gas, swept-up by the primary jet, where a shock front is generated as a consequence of the supersonic impact of the jet with the natal cloud. Shocks heat, accelerate and compress the ambient gas material switching on a complex chemistry that leads to an enhancement of the abundance of several species in the so-called “chemically active outflows” (e. g., Bachiller 1996). The nature and properties of these shocks are still not well under-

stood, in particular the role of the magnetic field. Water is predicted to be one of the main gas cooling agents in magnetized shocks, along with H₂ and CO (e. g., Draine et al. 1983; Kaufman & Neufeld 1996; Flower & Pineau Des Forêts 2010). Thanks to its rich emission spectrum, transitions spanning a wide range of excitation conditions, and its sensitivity to local conditions (e. g., Bergin et al. 1998; van Dishoeck et al. 2011), H₂O constitutes a powerful probe of the physics and chemistry of the shock outflow interaction. In particular, in shocked regions H₂O abundance can increase by several orders of magnitude, up to $\sim 10^{-4}$, through sputtering of grains mantles and formation in the gas phase at high temperatures (Hollenbach & McKee 1989; Kaufman & Neufeld 1996; Flower & Pineau Des Forêts 2010).

The outflow powered by the low-mass Class 0 protostar L1157-mm ($d \approx 250$ pc; Looney et al. 2007) displays a rich specific chemistry which makes it the prototype of “chemically active” outflows (e. g., Bachiller & Perez Gutierrez 1997; Bachiller et al. 2001; Arce et al. 2008). As such, it is an excel-

Send offprint requests to: Gemma Busquet,
e-mail: gemma.busquet@iaps.inaf.it

[★] Based on *Herschel* HIFI and PACS observations. *Herschel* is an ESA space observatory with science instruments provided by European-led Principal Investigator consortia and with important participation from NASA.

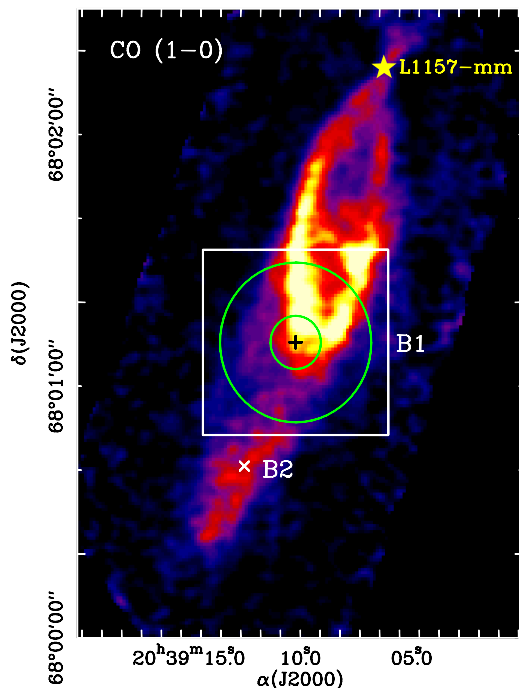


Fig. 1. Southern blueshifted outflow lobe observed in CO (1–0) with the Plateau de Bure Interferometer (PdBI) by Gueth et al. (1996). The black cross marks the nominal position of the bow-shock L1157-B1 while the tilted white cross indicates the nominal position of the B2 shock (Bachiller & Perez Gutierrez 1997). The largest ($\sim 38''$) and smallest ($\sim 12''.7$) HIFI main-beams are indicated with circles. The field of view of the PACS observations is displayed with a white box. The star depicts the position of the protostar L1157-mm.

lent laboratory to investigate the physical conditions and the formation routes of H_2O and its role in the cooling of a typical protostellar outflow. The L1157 outflow has been studied in detail for more than two decades through many molecular lines and in a wide range of wavelengths, from the near-infrared (e.g., Davis & Eisloffel 1995; Neufeld et al. 2009; Nisini et al. 2010b) to the radio domain (e.g., Zhang et al. 2000; Bachiller et al. 2001; Tafalla & Bachiller 1995). Several compact shocked regions are found along both the blue- and redshifted lobes (see e.g., Gueth et al. 1998; Nisini et al. 2007, 2010b). In particular, the southern blueshifted lobe, shown in Fig. 1, consists of two limb-brighened cavities each of them associated with a bow-shock, likely created by episodic events in a precessing jet (Gueth et al. 1996).

Water emission in L1157-B1 was first detected with ISO by Giannini et al. (2001); however, only three lines were detected and the physical conditions of H_2O could not be constrained. Later on, *Odin* and SWAS observed the fundamental o- H_2O line emission in the direction of the southern blueshifted lobe of the outflow (Bjerkeli et al. 2009; Franklin et al. 2008). The low angular resolution gave access only to properties averaged over the entire outflow lobe. Assuming that both the H_2O and the low- J CO line emission originate in the same gas, these authors inferred an o- H_2O abundance ranging between 10^{-6} and 2×10^{-4} . As part of the “Water In Star-forming regions with Herschel” (WISH) key program, Nisini et al. (2010a) used PACS to map the o- H_2O 179 μm line over the entire outflow structure. These authors detected extended emission, with several strong peaks

associated with shocked knots, well spatially correlated with H_2 rotational lines (Nisini et al. 2010b).

The molecular bright shock region B1, in the southern lobe of the outflow (see Fig. 1), was selected as one of the targets of the key program “Chemical Herschel Surveys of Star forming regions” (CHESs¹) dedicated to unbiased spectral line surveys of prototypical star-forming regions (Ceccarelli et al. 2010) in the guaranteed time of the *Herschel* Space Observatory (Pilbratt et al. 2010).

The CHESs survey of L1157-B1 offers a comprehensive view on the water line emission in a typical protostellar bow-shock, considered as the benchmark for shock models (Gusdorf et al. 2008a,b; Flower & Pineau Des Forêts 2010; Flower & Pineau des Forêts 2012). A grand total of 13 water lines (both ortho and para) have been detected across the submillimeter and far-infrared window with the PACS spectrometer (Poglitsch et al. 2010) and the HIFI heterodyne instrument (de Graauw et al. 2010), the largest data set of water lines detected so far in a protostellar shock. Both instruments provide us with a detailed picture on the kinematics and the spatial distribution of the water emission in L1157-B1, allowing us to derive strong constraints on the water abundance and the physical conditions in the emitting gas. The paper layout is as follows. In Sect. 2 we summarize our observations. In Sect. 3 we present the main results of HIFI and PACS and in Sect. 4 we analyze the excitation conditions of H_2O using a Large Velocity Gradient model and discuss the origin of the water emission in L1157-B1, presenting, for the first time, a detailed picture of the bow-shock structure through *Herschel* observations of water lines. Finally, in Sect. 5 we list the main conclusions.

2. Observations and data reduction

2.1. HIFI observations

The HIFI observations were performed in double beam switching mode during 2010 towards the nominal position of B1: $\alpha(J2000)=20^{\text{h}}39^{\text{m}}10^{\text{s}}.2$, $\delta(J2000)=68^{\circ}01'10''.5$. Both polarizations (H and V) were observed simultaneously. The receiver was tuned in double sideband (DSB). Most of the submillimeter window was covered in an unbiased way with HIFI, and the observations were carried out in spectral scanning mode. In order to study the properties of the H_2O gas in the high-velocity wings of the outflow, a few lines were observed in pointed mode in order to reach an excellent signal-to-noise ratio (SNR).

We used the Wide Band Spectrometer (WBS), which provides a frequency resolution of 0.5 MHz (i.e., velocity resolution between 0.1 km s^{-1} and 0.4 km s^{-1} , depending on the wavelength). The data were processed with the ESA-supported package *Herschel Interactive Processing Environment*² (HIPE, Ott 2010) version 6 package. After level 2 fits files were exported and transformed into GILDAS³ format for baseline subtraction and subsequent sideband deconvolution, which was performed manually. The relative calibration between both receivers (H and V) was found very good, and both signals were co-added in order to improve the noise rms of the data.

The spectral resolution was then degraded to a common velocity resolution of 1 km s^{-1} in the final single side band

¹ <http://www-laog.obs.ujf-grenoble.fr/heberges/chess>

² HIPE is a joint development by the *Herschel* Science Ground Segment Consortium, consisting of ESA, the NASA *Herschel* Science Center, and the HIFI, PACS and SPIRE consortia

³ See <http://www.iram.fr/IRAMFR/GILDAS>

Table 1. List of H₂O transitions^a observed with HIFI in L1157–B1. Peak intensity (in T_{mb} scale), peak velocity, and integrated intensity between -40 and $+2.6$ km s⁻¹ are reported. The uncertainties are indicated in parenthesis.

Transition	Frequency (GHz)	λ (μm)	E_u/k_B (K)	HPBW (arcsec)	η_{mb}	Obs_Id	rms ^b (mK)	T_{peak} (K)	v_{peak} (km s ⁻¹)	$\int T_{\text{mb}} dv$ (K km s ⁻¹)
o-H ₂ O 1 ₁₀ – 1 ₀₁	556.936	538.66	26.7	38.1	0.75	1342181160	8	1.04(0.16)	-1.9(0.3)	13.0(0.1)
3 ₁₂ – 3 ₀₃	1097.365	273.38	215.1	19.3	0.74	1342196453	26	0.29(0.04)	-2.0(0.3)	4.1(0.2)
3 ₁₂ – 2 ₂₁	1153.127	260.17	215.1	18.3	0.64	1342207691	39	0.18(0.03)	-1.9(0.1)	1.3(0.3)
3 ₂₁ – 3 ₁₂	1162.912	257.98	271.0	18.3	0.64	1342207691	36 ^c	0.11(0.03)	-1.7(0.4)	0.5(0.2)
2 ₂₁ – 2 ₁₂	1661.008	180.49	159.8	12.7	0.71	1342196538	138	0.36(0.14)	-1.7(0.1)	2.0(0.8)
2 ₁₂ – 1 ₀₁	1669.905	179.52	80.1	12.7	0.71	1342207689	56	0.94(0.14)	-5.5(0.3)	12.7(0.4)
p-H ₂ O 2 ₁₁ – 2 ₀₂	752.033	398.92	136.9	28.2	0.75	1342207611	20	0.46(0.07)	-3.6(0.3)	4.6(0.1)
2 ₀₂ – 1 ₁₁	987.927	303.67	100.8	21.5	0.74	1342207640	50	0.79(0.12)	-3.3(0.2)	11.0(0.3)
1 ₁₁ – 0 ₀₀	1113.343	269.47	53.4	19.1	0.74	1342207388	56	0.79(0.12)	-4.1(0.1)	11.1(0.4)

Notes. ^(a) Frequencies taken from the spectroscopic catalog JPL (Pickett et al. 1998). ^(b) Root mean square (rms) noise are given for an interval of 0.5 MHz. ^(c) Root mean square (rms) noise is given for an interval of 1.5 MHz.

Table 2. List of H₂O transitions^a detected with PACS in L1157–B1, at the nominal position of B1 (spaxel centered at offset (0'', 0'')) and at the high- J CO peak (spaxel at offset (-5'', 7'')).

Transition	Frequency (GHz)	λ (μm)	E_u/k_B (K)	HPBW (arcsec)	Flux ^b ($\times 10^{-17}$ W m ⁻² /pixel)		Line_Id
					offset (0'', 0'')	offset (-5'', 7'')	
o-H ₂ O 2 ₂₁ – 2 ₁₂	1661.008	180.49	159.8	12.7	2.6±0.2	2.7±0.3	1
2 ₁₂ – 1 ₀₁	1669.905	179.52	80.1	12.7	12.1±0.2	12.9±0.3	2
3 ₀₃ – 2 ₁₂	1716.769	174.63	162.5	12.3	6.2±0.3	6.5±0.3	3
4 ₂₃ – 4 ₁₄	2264.149	132.41	397.9	9.4	<0.6 ^c	0.6±0.2	4
4 ₁₄ – 3 ₀₃ ^d	2640.474	113.54	289.2	8.0	2.8±0.5	3.7±0.4	5
2 ₂₁ – 1 ₁₀	2773.978	108.07	159.8	7.6	3.2±0.4	3.9±0.5	6
3 ₂₁ – 2 ₁₂	3977.046	75.38	271.0	5.3	<2.1 ^c	1.9±0.7	7
p-H ₂ O 3 ₁₃ – 2 ₀₂	2164.132	138.53	204.7	9.8	2.7±0.3	2.7±0.3	8
4 ₀₄ – 3 ₁₃	2391.573	125.35	319.5	8.9	1.1±0.3	1.4±0.3	9

Notes. ^(a) Frequencies taken from the spectroscopic catalog JPL (Pickett et al. 1998). ^(b) Line fluxes obtained with a Gaussian fit of the line profile. ^(c) 3σ upper limit based on the rms estimated at offset (-5'', 7''). ^(d) This line is blended with the CO (23–22) transition. To estimate the flux of the water line we subtracted the flux of CO (23–22) transition predicted by the model presented in Benedettini et al. (2012).

(SSB) data set. Uncertainty in the flux calibration were estimated to be $\sim 20\%$. In Table 1 we summarize the observational parameters of the H₂O transitions detected with HIFI (frequency, wavelength, upper level energy). The main-beam intensity, peak velocity, and the integrated intensity for each transition are also reported. Intensities are expressed in units of main-beam brightness temperature. The telescope parameters (half power beamwidth (HPBW) and main-beam efficiency (η_{mb})) are taken from Roelfsema et al. (2012).

2.2. PACS observations

The PACS observations were carried out on May 25th, 2010 in line spectroscopy mode in order to obtain a full range spectrum of the molecular line emission towards B1, from 55–95.2 μm and from 101.2–210 μm . The spectral scan was centered at the nominal position of B1 (see above) and produced a single 5×5 spectral map of $9''.4$ square spatial pixels (hereafter spaxels) over a $47'' \times 47''$ field of view. Two observations were conducted for the 161.5–190.2 μm range. Both measurements are in good agreement, with a discrepancy at the most $\sim 10\%$. The resolving power ranges from 1000 to 4000 (i. e., spectral resolution of ~ 75 –300 km s⁻¹) depending on the wavelength, hence water lines are unresolved. PACS data were processed with HIPE version 5.0. The absolute flux scale was determined from obser-

vations of Neptune by normalizing the observed flux to the telescope background, with an estimated uncertainty of $\sim 10\%$ for $\lambda < 190 \mu\text{m}$ (i. e., where all the water PACS lines lie). Further details of the PACS observations are described in Benedettini et al. (2012), where the emission lines of CO, OH, and [OI] lines are presented and discussed.

In Table 2 we list the detected transitions, giving their frequency, wavelength, upper energy level, and beam size. We extracted the flux toward each spaxel adopting a Gaussian instrumental response. The line fluxes measured toward the two brightest spaxels, at offsets (0'', 0'') and (-5'', 7''), associated with the nominal position of B1 and the high-excitation CO emission peak (Benedettini et al. 2012), respectively, are reported in Table 2.

2.3. Cross calibration

Four lines were observed by both PACS and HIFI instruments, which allowed us to check the consistency of the calibration: H₂O (2₁₂–1₀₁) at 179 μm , (2₂₁–2₁₂) at 180 μm , CO (16–15), and CO (14–13). Using the PACS maps, we estimated the line intensities in the HIFI main-beam solid-angle towards the nominal position of B1. Comparison of the HIFI- and PACS-based line intensities shows a very good agreement for H₂O (2₁₂ – 1₀₁) and CO (14–13), where the integrated intensities

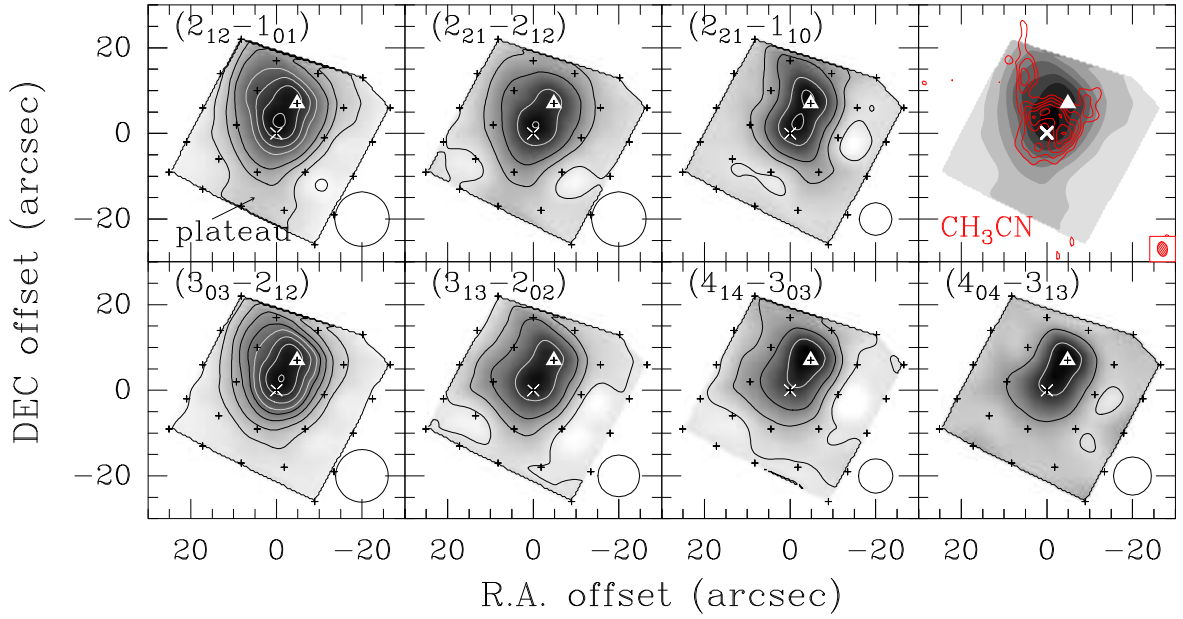


Fig. 2. PACS maps of H_2O line fluxes (increasing upper level energy from top left to bottom right). First contour corresponds to 1σ flux level of each transition. Contours step is 2σ in all lines except for the $\text{o-H}_2\text{O}$ ($2_{12} - 1_{01}$) and $\text{o-H}_2\text{O}$ ($3_{03} - 2_{12}$), for which contours step is 6σ and 3σ , respectively, where σ is listed in Table 2. The top right panel shows an overlay of the $\text{o-H}_2\text{O}$ ($2_{12} - 1_{01}$) map (grey scale) with the PdBI CH_3CN ($8-7$) $K=0-2$ image (red contours) from Codella et al. (2009) tracing the bow-shock. The synthesized beam of PdBI, $3''.4 \times 2''.3$ (P. A. = 10°), is shown in the bottom right corner of this panel. Crosses mark the central position of each spaxel of the PACS field of view. The white triangle indicates the position of CO peak traced by high- J_{up} PACS lines (Benedettini et al. 2012) and the tilted cross depicts the nominal position of the B1 shock. The Half Power Beam Width (HPBW) of each transition is indicated in the bottom right corner of each panel and listed in Table 2.

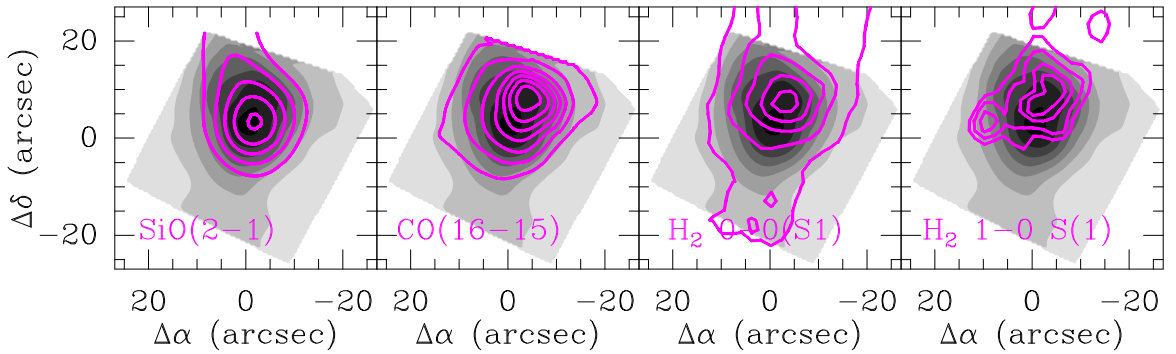


Fig. 3. Contour maps of the SiO ($2-1$) high-velocity ($v < -8 \text{ km s}^{-1}$) emission from Gueth et al. (1998) convolved to the $12''.7$ PACS resolution, the CO ($16-15$) line observed with PACS (Benedettini et al. 2012), H_2 $0-0$ S(1) from Nisini et al. (2010b), and H_2 $1-0$ S(1) from Caratti o Garatti et al. (2006), overlaid on the H_2O ($2_{12} - 1_{02}$) map at $179 \mu\text{m}$ (grey scale). In each panel the transition in contours is indicated.

are $13.7/14.2 \text{ K km s}^{-1}$ and $5.0/5.5 \text{ K km s}^{-1}$, respectively (for HIFI/PACS instruments), resulting in a discrepancy of $\sim 10\%$. For the H_2O ($2_{21} - 2_{12}$) and CO ($16-15$) lines, the HIFI/PACS integrated intensities are $2.0/1.8 \text{ K km s}^{-1}$ and $3.4/2.7 \text{ K km s}^{-1}$, respectively. For these lines the discrepancy is larger, about $\sim 20\%$, but always within the absolute flux calibration uncertainty. We note that both lines are weaker, and the SNR of the data much lower than the other two lines. Overall, we conclude that the agreement between the HIFI and PACS calibration scales is very good.

3. Results

We have detected 13 H_2O transitions with a flux above the 5σ level: 7 H_2O transitions (5 ortho, 2 para) in the PACS range ($55-210 \mu\text{m}$), 8 H_2O transitions (5 ortho, 3 para) with HIFI between $672 \mu\text{m}$ and $180 \mu\text{m}$. Note that the $179 \mu\text{m}$ and $180 \mu\text{m}$ lines have been detected with both instruments. The $\text{o-H}_2\text{O}$ ($3_{21} - 3_{12}$) transition is detected at a 3σ level with HIFI (see Table 1). Two additional $\text{o-H}_2\text{O}$ transitions ($3_{21} - 2_{10}$ at $75.38 \mu\text{m}$ and $4_{23} - 4_{14}$ at $132.41 \mu\text{m}$) are tentatively detected with PACS at the 3σ level at the offset position ($-5''$, $7''$) (see Table 2). Overall, we detected only transitions of rather low E_{u} , with values ranging between 26.7 K and 319.5 K .

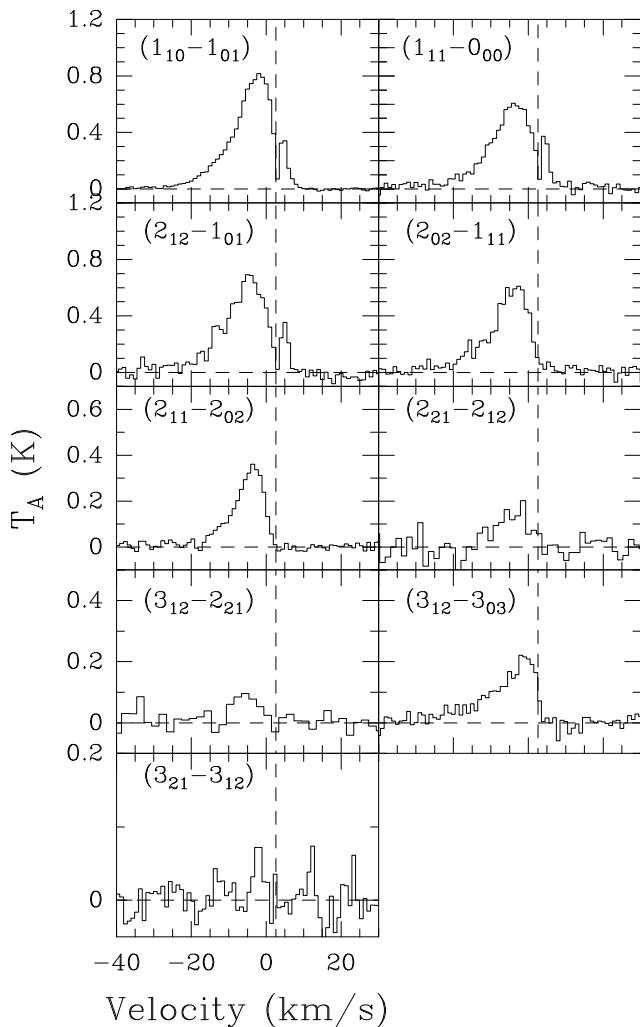


Fig. 4. HIFI H₂O spectra of L1157-B1 smoothed to a velocity resolution of 1 km s⁻¹. The H₂O transition is indicated in each panel. The vertical dashed line marks the ambient LSR velocity $v_{\text{LSR}} \sim 2.6$ km s⁻¹ from C¹⁸O emission (Bachiller & Perez Gutierrez 1997).

3.1. H₂O spatial distribution

Maps of o-H₂O and p-H₂O lines observed with PACS are presented in Fig. 2. Water is detected over the entire outflow cavity, both upstream and downstream of the bow-shock; its distribution overlaps rather well with the B1 bow-shock as traced by CH₃CN (Codella et al. 2009, see top right panel) and the outflow walls of the B1 cavity, traced by CO at the PdBI (Gueth et al. 1996, see Fig. 1). Downstream of B1, weak emission is present 20'' away from the shock in several transitions, including the 3₀₃–2₁₂ and 2₁₂–1₀₁ lines, in agreement with Nisini et al. (2010a). This extended emission, which consists of a plateau of low H₂O brightness, is related to the outflow, possibly from the B2 outflow cavity.

Leaving aside the contribution of the plateau to the emission, the distribution of the water emission in B1 displays little variation between the various transitions, with a typical deconvolved size at Full-Width at Half Maximum (FWHM) of $\sim 10''$. Overall, the emission appears elongated along the major outflow axis. The H₂O brightness peak is located $\approx 6''$ north of the center of the PACS array, lying approximately halfway between the

nominal position of B1 and the high- J CO emission peak identified by Benedettini et al. (2012), at the interface between spaxels (2,2) and (3,2) at offsets (0'', 0'') and (-5'', 7''), respectively. However, size and position determination from the PACS under-sampled data are just indicative and they suffer large uncertainties.

It is interesting to compare the morphology of the 2₁₂–1₀₁ line with that of other shock tracers (see Fig. 3). One can see that both H₂O and SiO peak at the same position, between offset (0'', 0'') and (-5'', 7''). Similar to H₂O, the emission of the mid-IR H₂O–0 S(1) pure-rotational line observed with *Spitzer* (Nisini et al. 2010b) is extended, partly tracing the B1 cavity, while CO(16–15) and the near-IR H₂ 1–0 S(1) rovibrational line (Caratti o Garatti et al. 2006) are rather compact and peak at offset (-5'', 7''), coinciding with the partly dissociative shock driven by the impact of the jet against the B1 cavity (Benedettini et al. 2012). However, it is worth noting that there is also bright H₂O emission at the peak of the high- J CO position, suggesting that part of the H₂O emission coincides with CO. The good match between SiO(2–1) and H₂O(2₁₂–1₀₁), both in terms of spatial distribution and the line profiles in the high-velocity range (see Fig. 2-b of Lefloch et al. 2012), provides us with an estimate of the size of the water line emission, $\approx 10''$, consistent with the PACS determination.

3.2. Line profiles

Figure 4 shows a montage of the water line spectra observed with HIFI smoothed to a velocity resolution of 1 km s⁻¹. Water line profiles are rather broad, with a FWHM ~ 10 km s⁻¹. The bulk of the emission in all transitions is clearly *blueshifted* with respect to the cloud systemic velocity $v_{\text{LSR}} = +2.6$ km s⁻¹ (Bachiller & Perez Gutierrez 1997). For lines with a SNR high enough, e. g., 3₁₂–3₀₃, 3 σ emission is detected at velocities up to -30 km s⁻¹.

The coexistence of multiple excitation components in L1157-B1 has been studied recently by Lefloch et al. (2012), who showed, based on the spectral slope, that the CO line emission arises from three different emitting regions. These components were tentatively identified as the jet impact shock region (g_1), the cavity walls of the L1157-B1 bow-shock (g_2), and the cavity walls from the earlier ejection episode that produced the L1157-B2 bow-shock (g_3). An schematic view of all these components is presented in Fig. 7. The authors showed that each component is characterized by an specific excitation temperature. We found that the profile of the o-H₂O(3₁₂–3₀₃) transition follows the same specific spectral signature observed for the CO(16–15) line profile (see Fig. 2-b of Lefloch et al. 2012), which is defining the g_1 component.

Despite the different beam sizes of the HIFI lines, Figure 5 shows a good match between the profiles of the water lines 2₁₁–2₀₂ at 752 GHz and 2₀₂–1₁₁ at 988 GHz, and between 1₁₁–0₀₀ at 1113 GHz and 2₁₂–1₀₁ at 1669 GHz, respectively. This defines two groups of water lines, each of them following a specific pattern suggesting that the lines within each group arise from the same region. Whereas the lines at 1669 GHz and 1113 GHz both peak at -5 km s⁻¹, the lines at 752 GHz and 988 GHz peak at -3 km s⁻¹.

A narrow dip ($\Delta v = 1.4$ km s⁻¹) is observed at the systemic cloud velocity $v_{\text{LSR}} = 2.6$ km s⁻¹ in the spectra of the three transitions that connect with the ground state level resulting in a double-peak profile (see Fig. 4 and Sect. 4.3 for further details).

Weak redshifted emission is detected in these transitions *only*, up to velocities of $+10$ km s⁻¹. Bjerkerli et al. (2013)

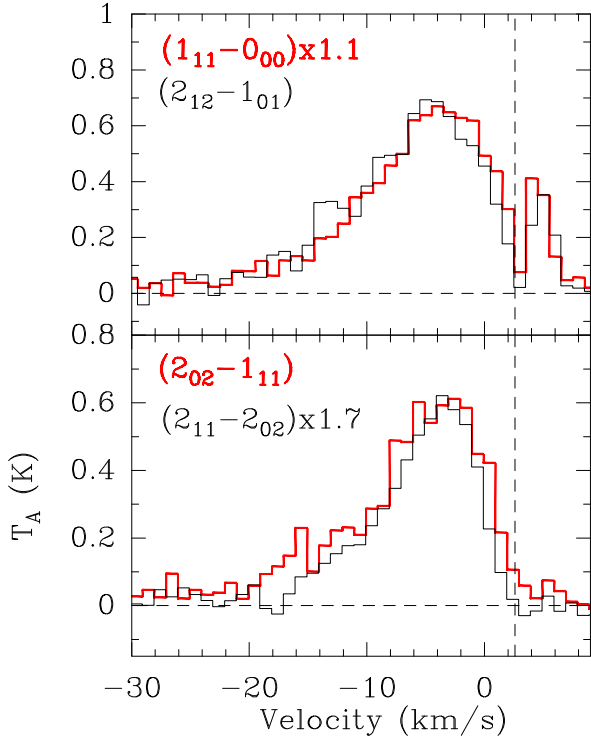


Fig. 5. Comparison of HIFI $\text{H}_2\text{O}(2_{12} - 1_{01})$ and $(1_{11} - 0_{00})$ lines (*top*) at 1669 GHz and 1113 GHz, respectively, and between the $\text{H}_2\text{O}(2_{02} - 1_{11})$ at 988 GHz and the $(2_{11} - 2_{02})$ at 752 GHz lines (*bottom*). The H_2O transitions are labeled in each panel. The vertical dashed line marks the ambient LSR velocity $v_{\text{LSR}} \sim 2.6 \text{ km s}^{-1}$ (Bachiller & Perez Gutierrez 1997).

showed that this weak redshifted emission is extended all over the southern outflow lobe. It is worth noting that this redshifted emission is also detected in the low- J HCN and HCO^+ lines (Bachiller et al. 2001; Benedettini et al. 2007). The lack of emission in other tracers such as CS, CH_3OH , H_2CO , or SiO suggests that this component has different excitation conditions from the main, blueshifted outflow component. The redshifted emission most likely arises from material located on the rear side of the cavity.

3.3. Outflow emission

Figure 6 (top panel) shows that the profile of the $\text{o-H}_2\text{O}(1_{10} - 1_{01})$ line at 556.9 GHz presents a significant excess of emission at low velocities compared with the two other lines connecting the ground state level (the $2_{12} - 1_{01}$ at 1669 GHz and the $1_{11} - 0_{00}$ at 1113 GHz transitions) that display similar line profiles (see Fig. 5). This is a priori surprising as the lines at 1113 GHz and 1669 GHz are sensitive to somewhat different excitation conditions.

We subtracted the profile of the $\text{p-H}_2\text{O}(1_{11} - 0_{00})$ line from the $\text{o-H}_2\text{O}(1_{10} - 1_{01})$ line and show its residual emission in Fig. 6 (thick spectrum in the top panel). This residual emission has a peak intensity of $T_{\text{mb}} \approx 0.38 \text{ K}$ and it peaks at $v = 0 \text{ km s}^{-1}$. This component spans a relatively narrow range of velocities, from $\sim 2.6 \text{ km s}^{-1}$ up to -8 km s^{-1} , and its integrated intensity, in T_{mb} scale, is 2.3 K km s^{-1} .

As can be seen in Fig. 1, the HIFI beam at 1113 GHz and 1669 GHz collects emission from a region at the apex of the

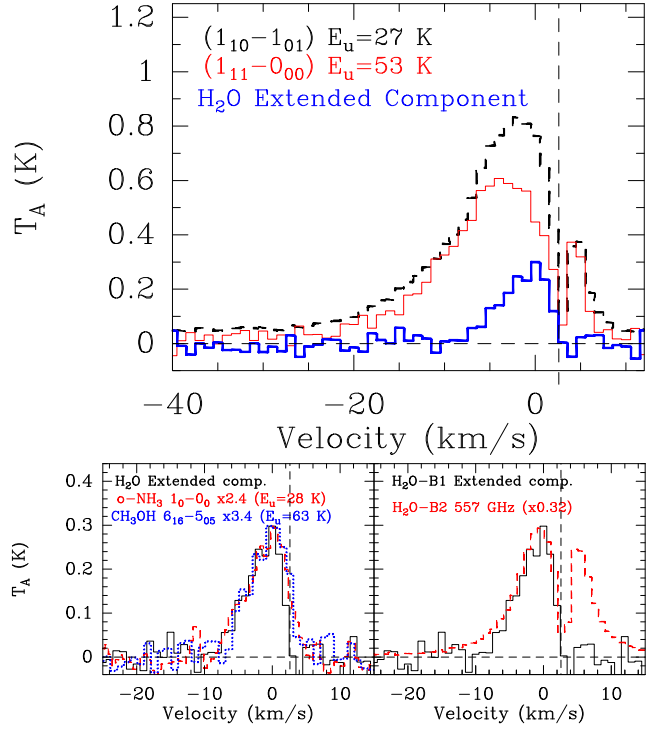


Fig. 6. *Top:* Comparison of HIFI spectra for H_2O transitions connecting with the ground state: $\text{o-H}_2\text{O}(1_{10} - 1_{01})$ shown by the dashed black line and $\text{p-H}_2\text{O}(1_{11} - 0_{00})$ shown by the thin red solid line. The spectrum shown in blue (solid thick line) is the residual emission after subtracting the emission of $\text{p-H}_2\text{O}(1_{11} - 0_{00})$ line from the $\text{o-H}_2\text{O}(1_{10} - 1_{01})$, referred to as extended component. *Bottom:* Comparison of the extended component seen in the $\text{H}_2\text{O}(1_{10} - 1_{01})$ line (black solid line) with the $\text{o-NH}_3(1_0 - 0_0)$ (red dashed line) and the $\text{CH}_3\text{OH}(6_{16} - 5_{05})$ (blue dotted line) spectra obtained from Codella et al. (2010) (left panel). Comparison of the $\text{o-H}_2\text{O}(1_{10} - 1_{01})$ line at 556.9 GHz observed in B1 (extended component; black solid line) and in L1157-B2 (red dashed line) from Vasta et al. (2012). In all panels the vertical dashed line marks the ambient LSR velocity $v_{\text{LSR}} \sim 2.6 \text{ km s}^{-1}$ (Bachiller & Perez Gutierrez 1997).

bow-shock, with a typical size of $\approx 10''$ (see also Lefloch et al. 2012) whereas the 556.9 GHz actually collects also emission associated with the B1 cavity walls and the entrained gas, downstream and eastward of the B1 cavity, associated with the B2 ejection. An additional clue on the origin of the extended component is obtained by comparing the 556.9 GHz line profiles of the extended component and the older outflow cavity L1157-B2 (see also Fig. 1) observed by Vasta et al. (2012). As can be seen in Fig. 6 (bottom right panel), both profiles show an excellent match at blueshifted velocities, suggesting a common origin. Interestingly, an excellent match was observed in the $\text{CO } J = 3 - 2$ profiles of the g_3 component and the L1157-B2 shock by Lefloch et al. (2012). Comparison of the line profile of the extended H_2O component with the $\text{o-NH}_3(1_0 - 0_0)$ and $\text{CH}_3\text{OH}(6_{16} - 5_{05})$ lines (Codella et al. 2010), observed at a similar angular resolution with HIFI ($\sim 38''$), reveals a very good agreement, supporting the hypothesis that they have a common origin and all trace the same gas. We propose that the broad HIFI beam at 556.9 GHz is actually tracing an extended component, of low excitation, for which the beam of HIFI is less sensitive to at the frequency of the H_2O lines at 1113 GHz (1669 GHz), as its

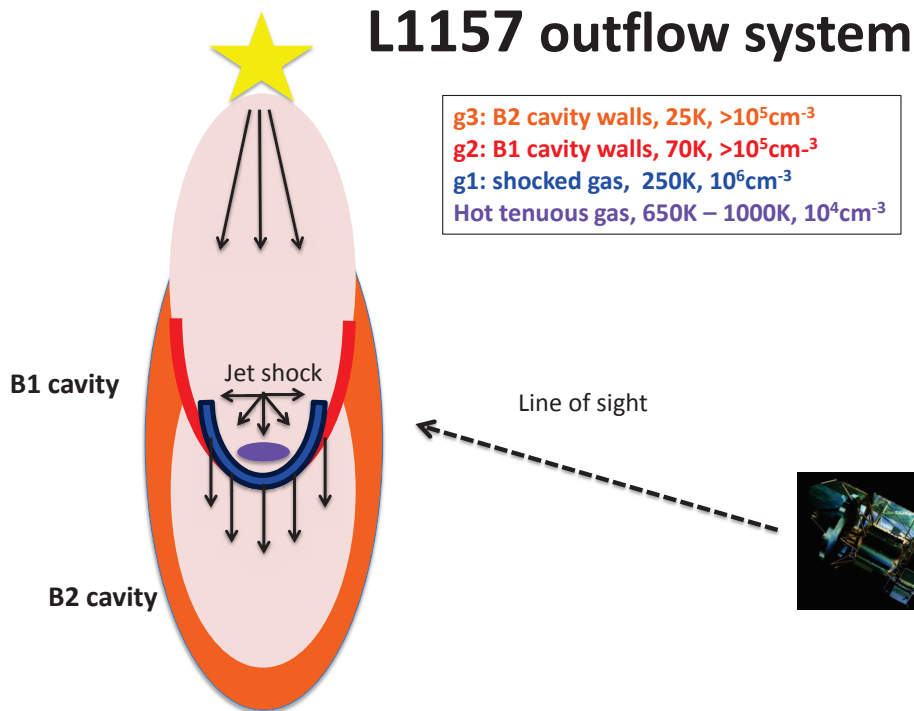


Fig. 7. Sketch of the L1157 blue-lobe outflow system. The B1 and B2 outflow cavities are indicated in red and orange, respectively. The two shock components identified through H_2O lines are displayed in blue (warm shocked gas) and in light violet for the hot tenuous gas. In the top right corner of the image we report on the physical conditions of each component. The observer, represented by the *Herschel* satellite, is indicated to the right side of the image.

size decreases from $38''$ to $19''.1$ ($12''.7$). Such a component could represent the counterpart at 556.9 GHz of the plateau evidenced by PACS, south of B1. Lack of angular resolution prevents from being more specific about the origin of the extended component, and a comparison with the 556.9 GHz map presented by Bjerkeli et al. (2013) would help to support our interpretation.

The H_2O emission from the outflow has been recently analyzed by Bjerkeli et al. (2013), who presented a detailed study of the physical properties (molecular mass, dynamical time-scale, momentum, kinetic energy, etc) in the outflow using CO and H_2O lines. In what follows, we will concentrate on the physical conditions in the bow-shock, where the bulk of H_2O emission originates from.

4. Analysis and discussion

We have determined the physical conditions of the B1 shock region from modelling the water line emission using a radiative transfer code in the Large Velocity Gradient (LVG) approximation. It is worth noting that the B1 shock position is about 1.5 far away from the protostar L1157-mm; the continuum emission detected in the submm/far-IR range is faint enough that infrared radiative pumping of the H_2O lines can be neglected.

We first present our approach to the modelling of the L1157-B1 emission (Sect. 4.1), we then discuss the best-fit solution to the emission from the B1 shock (Sect. 4.2), and we show its consistency with the previous works on CO and H_2 . We assess the influence of various parameters of the modelling, in particular the actual value of the ortho to para H_2 ratio in the shocked

gas. Finally, we study the origin of the water absorbing layer in the cloud (Sect. 4.3), and report on the water abundance and far-IR cooling (Sect. 4.4). For the sake of clarity, we display in Fig. 7 the physical structure emerging from our H_2O line study that summarizes the main results to be presented in this section. Briefly, we identified five components: the cloud seen in absorption, the outflow material from the B1 (g_2) and B2 (g_3) cavities, the jet impact shock region (g_1) and a compact hot gas component.

4.1. Modelling

Previous studies at millimeter and infrared wavelengths (Benedettini et al. 2007; Codella et al. 2009; Takami et al. 2011, and more recently Benedettini et al. 2013) reveal a complex density, temperature, and velocity structure, with several emission knots of shocked gas in various tracers. In such complex environment, a comprehensive modelling of the water line emission from the bow-shock, notoriously a very difficult task, is just a problem too difficult to handle if one consider the angular resolution of the data (at best comparable to the size of the region), the one-dimensional nature of the source geometrical modelling, and the radiative transfer code used. Our goal here is to identify the main shock components responsible for the H_2O emission detected, and, within the uncertainties inherent to the calibration and geometry adopted, the physical conditions of these components.

The PACS maps (Fig. 2) show that the H_2O emission does not peak at the nominal position of B1, where the HIFI beam is

centered; the larger HIFI beams encompass the emission peak while for the smaller HIFI beams the peak is partially covered (see Fig. 1). It is all the more important to carry out LVG calculations using water fluxes measured over the same source solid angle; we therefore convolved all the PACS maps to a common angular resolution of $12''.7$ to measure the flux towards the nominal position of B1. For the HIFI lines, we convolved the o-H₂O ($2_{12} - 1_{01}$) PACS map at the resolution of the different HIFI beams. Assuming that all HIFI lines have the same spatial distribution as the o-H₂O ($2_{12} - 1_{01}$) line we can then derive the HIFI beam filling factor. As a test, we compared the beam filling factors obtained from PACS maps of the 108, 138, and 125 μm lines. In practice, we obtain very similar correcting factors, which made us feel confident in the robustness of the procedure and the results obtained. The fluxes of all the H₂O lines estimated in a beam of $12''.7$ are listed in Table 3.

We investigated the excitation conditions of the H₂O line emission using a radiative transfer code in the LVG approximation (Ceccarelli et al. 2003) and adopting a plane parallel geometry. The molecular data were taken from the BASECOL⁴ database (Dubernet et al. 2006, 2013) and we used the new collisional rate coefficients with H₂ (Dubernet et al. 2009; Daniel et al. 2010, 2011). The linewidth (FWHM of the line profile) was set to a fixed value of 10 km s⁻¹. The model includes the effects of the beam filling factor, and it computes the reduced chi-square χ_r^2 for each column density minimizing with respect to the source size, kinetic temperature, and density. We adopted an uncertainty in the integrated intensities of 30% for all line except the HIFI lines with high E_u and the PACS lines lying at the edges of the band, for which the adopted uncertainty is 50%.

4.2. Shock emission: best-fit model

4.2.1. A two-temperature model

The present LVG calculations were carried out for an ortho-para ratio (OPR) of 0.5 in the H₂ gas, which is close to the value estimated by Nisini et al. (2010b) for gas in the same range of excitation conditions from modelling the H₂ emission, and an OPR of the H₂O gas equal to 3. We also adopted a size of $10''$, as estimated from the PACS maps, consistent with our previous findings (Benedettini et al. 2012) and with the *Spitzer* image of L1157-B1 observed in the H₂ lines (Nisini et al. 2010b) and in the IRAC bands (Takami et al. 2011).

To account for the line fluxes of the three transitions connected to the ground state (ortho and para) and assuming a source size of $10''$, the acceptable range of physical condition is $T_{\text{kin}} \sim 200\text{--}300$ K, $n(\text{H}_2) = (1 - 6) \times 10^6$ cm⁻³, and $N(\text{o-H}_2\text{O}) = (0.8 - 2) \times 10^{14}$. The best-fit model yields a warm gas component at 250 K, $n(\text{H}_2) = 1 \times 10^6$ cm⁻³, $N(\text{o-H}_2\text{O}) = 2 \times 10^{14}$ cm⁻². These physical conditions are absolutely unable to account for the flux of lines at higher upper energy levels (see Fig. 8-top panel).

A second gas component, at a much higher temperature and lower density, is needed to reproduce the flux detected in the higher E_u transitions. Solutions with $T_{\text{kin}} \approx 650$ K, $N(\text{o-H}_2\text{O}) = 1 \times 10^{17}$ cm⁻², $n(\text{H}_2) = 8 \times 10^3$ cm⁻³, and a source size of $4''$, are possible, in principle, under the assumption that the OPR-H₂ remains unchanged, equal to 0.5. Observational constraints on H₂ suggest a higher value of OPR-H₂, typically ≈ 3 , at high temperatures (see below). Assuming a typical OPR-H₂ of 3 for the second, hot gas component, our modelling

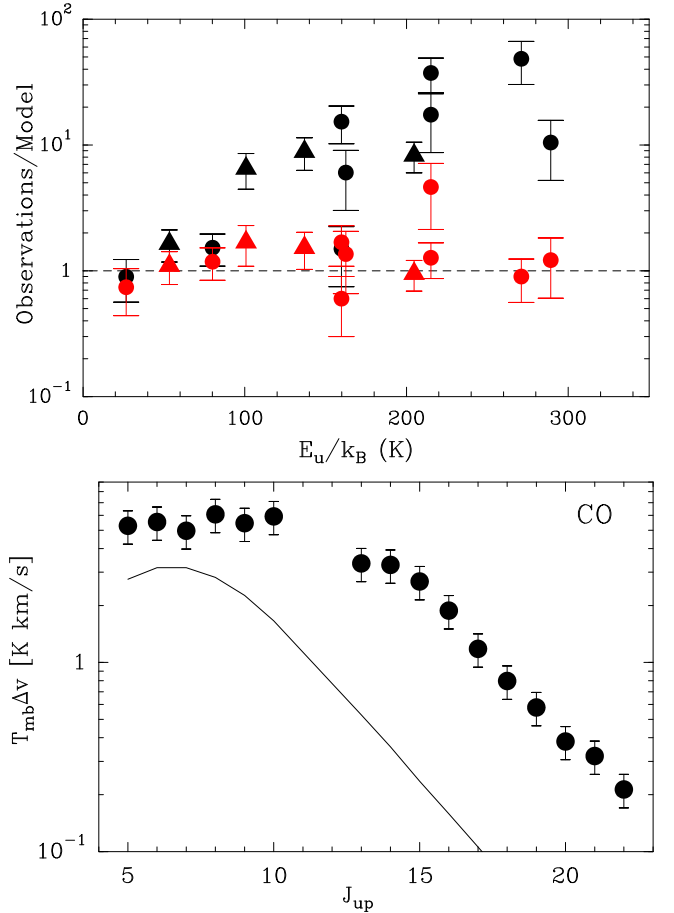


Fig. 8. *Top:* ratio between the measured integrated intensities and the LVG model predictions. Filled circles/triangles depict o-H₂O and p-H₂O lines, respectively. In black, we display the results assuming one single temperature component ($T_{\text{kin}}=250$ K, $n(\text{H}_2)=10^6$ cm⁻³, $N(\text{o-H}_2\text{O})=2 \times 10^{14}$ cm⁻², size= $10''$). In red, the final solution when adding the contribution of the second temperature ($T_{\text{kin}}=1000$ K, $n(\text{H}_2)=2 \times 10^4$ cm⁻³, $N(\text{o-H}_2\text{O})=7 \times 10^{16}$ cm⁻², size= $2''.5$). *Bottom:* predicted CO fluxes from the **hot** component, as a function of the rotational upper level in the HIFI and PACS range. The observed fluxes (Benedettini et al. 2012; Lefloch et al. 2012) are marked with filled circles. The choice of $[\text{CO}]/[\text{H}_2\text{O}]=1$ provides an upper limit estimate of the CO integrated intensity (see Sect. 4.2.3 for more details).

favors higher-temperature solutions, with $T_{\text{kin}} \approx 1000$ K, $N(\text{o-H}_2\text{O}) = 7 \times 10^{16}$ cm⁻², $n(\text{H}_2) = 2 \times 10^4$ cm⁻³, and a size of $2''.5$ as a best-fit model. We found, however, a range of possible solutions, with $T_{\text{kin}} \sim 900\text{--}1400$ K, $N(\text{o-H}_2\text{O}) = (3 - 7) \times 10^{16}$ cm⁻², $n(\text{H}_2) = (0.8 - 2) \times 10^4$ cm⁻³, and a size of $2''\text{--}5''$.

Therefore, a small region of hot, low density gas is contributing in addition to the warm dense g_1 gas, to the water emission detected by Herschel.

To evaluate the quality of our best-fit model, we have computed the ratio of the measured water line fluxes to those predicted by our model as a function of the upper energy level of the transition. As can be seen in Fig. 8-top panel, the overall agreement between the measured fluxes and the observations is satisfying; indeed a χ_r^2 minimization of our two-temperature model yields $\chi_r^2 = 1.0$. The water line fluxes resulting from the LVG

⁴ <http://basecol.obspm.fr>

Table 3. Observed and predicted water line fluxes for an OPR $\text{H}_2\text{O}=3$. Uncertainties are indicated in parenthesis.

Line	Freq. (GHz)	λ (μm)	E_u/k_B (K)	Flux[12.7''] ^a (K km s ⁻¹)	LVG predictions		
					Comp. 1-Warm ^b (K km s ⁻¹)	Comp. 2-Hot ^c (K km s ⁻¹)	Total (K km s ⁻¹)
o-H₂O							
1 ₁₀ – 1 ₀₁	556.936	538.66	26.7	35.0(13.0) ^d	39.0	8.3	47.3
3 ₁₂ – 3 ₀₃	1097.365	273.38	215.1	6.0(2.0)	0.3	1.0	1.3
3 ₁₂ – 2 ₂₁	1153.127	260.17	215.1	1.9(0.9)	0.05	1.4	1.5
3 ₂₁ – 3 ₁₂	1162.912	257.98	271.0	0.8(0.4)	0.02	0.9	0.9
2 ₂₁ – 2 ₁₂	1661.008	180.49	159.8	3.0(1.0)	0.2	1.6	1.8
2 ₁₂ – 1 ₀₁	1669.905	179.52	80.1	14.0(4.0)	9.2	2.7	11.9
3 ₀₃ – 2 ₁₂	1716.770	174.62	162.5	6.0(2.0)	1.0	3.4	4.4
4 ₁₄ – 3 ₀₃	2640.474	113.54	289.3	0.6(0.3)	0.06	0.4	0.5
2 ₁₂ – 1 ₁₀	2773.977	108.10	159.9	0.6(0.2)	0.4	0.6	1.0
p-H₂O							
2 ₁₁ – 2 ₀₂	752.033	398.92	136.9	11.4(3.3)	1.3	6.2	7.5
2 ₀₂ – 1 ₁₁	987.927	303.67	100.8	19.0(6.0)	2.9	8.4	11.3
1 ₁₁ – 0 ₀₀	1113.343	269.47	53.4	21.0(6.0)	12.8	6.3	19.1
3 ₁₃ – 2 ₀₂	2164.132	138.54	207.7	1.1(0.3)	0.1	1.0	1.1

Notes. ^(a) Corrected fluxes obtained for a common angular resolution of 12''. ^(b) LVG predicted fluxes for the best-fit model of the warm component ($T_{\text{kin}}=250$ K, $n(\text{H}_2)=10^6$ cm⁻³, $N(\text{o-H}_2\text{O})=2\times 10^{14}$ cm⁻², $N(\text{p-H}_2\text{O})=7.0\times 10^{15}$ cm⁻², and a source size of 10'') and using an OPR H_2 of 0.5 (see Sect. 4.2.1. and 4.2.2). ^(c) LVG predicted fluxes for the best-fit model of the hot component ($T_{\text{kin}}=1000$ K, $n(\text{H}_2)=2\times 10^4$ cm⁻³, $N(\text{o-H}_2\text{O})=7\times 10^{16}$ cm⁻², $N(\text{p-H}_2\text{O})=2.1\times 10^{16}$ cm⁻², and a source size of 2'') and using an OPR H_2 of 3 (see Sect. 4.2.1. and 4.2.2). ^(d) Flux after removing the contribution of the extended component detected in the 556.9 GHz line (see Sect. 3.3).

Table 4. Physical conditions of the shock components accounting for the water line emission in L1157-B1.

Comp.	T_{kin} (K)	$n(\text{H}_2)$ (cm ⁻³)	$N(\text{H}_2\text{O})$ (cm ⁻²)	$N(\text{H}_2)$ (cm ⁻²)	$X(\text{H}_2\text{O})$	Size ('')	$L(\text{H}_2\text{O})$ (L_{\odot})	$L(\text{CO})$ (L_{\odot})	$[\text{H}_2\text{O}]/[\text{CO}]$
Warm	250– 300	(1–3) $\times 10^6$	(1.2–2.7) $\times 10^{14}$	1.2×10^{20}	(0.7–2.0) $\times 10^{-6}$	10	0.002	0.004	0.03
Hot	900–1400	(0.8–2) $\times 10^4$	(4.0–9.1) $\times 10^{16}$	3.3×10^{20}	(1.2–3.6) $\times 10^{-4}$	2–5	0.03	0.01	1

modelling are reported in Table 3 and the range of physical conditions of the warm (g_1) and hot shock gas components are summarized in Table 4. The large number of lines detected at high SNR together with the availability of a wealth of complementary data allow us to constrain the water excitations conditions with unprecedented precision. It is important, however, to remark that source sizes have been imposed and this two-component model is a simplification of the complex structure of the bow-shock, in which, most likely, a wide and continuous range of temperatures and densities are present.

Finally, we evaluated the influence of the OPR- H_2O on the results. Only models with an OPR- H_2O of 3 (the statistical equilibrium value) can match the observed line fluxes while a value of 1 always yields solutions with a $\chi_r^2 > 2$.

4.2.2. Influence of the ortho-to-para H_2 ratio

In their study of the emission of the pure rotational lines of H_2 with *Spitzer*, Nisini et al. (2010b) found evidence for two gas components at ≈ 300 K and 1400 K, respectively. They modeled the OPR- H_2 as varying continuously from a value of ≈ 0.6 in gas at 300 K to its value at LTE (= 3) in gas at 1400 K. Therefore, we explored the range of acceptable solutions (n , N , T) when considering OPR- H_2 as a free parameter. The best-fit solution was obtained for an OPR of 0.5 in the gas at 250 K, hence a value similar to that found by Nisini et al. (2010b) in the gas of moderate excitation. We could not find any reasonable set of physical

conditions for values of OPR- H_2 higher than 1 for that component.

As noticed by Wilgenbus et al. (2000), such a low value of the OPR- H_2 indicates that the gas has been recently heated up by the passage of the shock front, and not affected by an older shock episode since the timescale between shock episodes is much less than the time needed for the OPR- H_2 to return to the equilibrium value. This is consistent with the youth of B1, for which the estimated dynamical age is ~ 2000 yr (Gueth et al. 1996) and the evolutionary age of the shock model presented by Gusdorf et al. (2008b). Low values of the OPR- H_2 have been reported in other outflow shock regions (e. g., Neufeld et al. 1998, 2006; Lefloch et al. 2003; Maret et al. 2009).

As for the second, hot gas component contributing to the water line emission, higher-temperature solutions are favored when adopting an OPR- H_2 of 3, and we found satisfying solutions ($\chi_r^2=0.8-1.2$) for $T_{\text{kin}}\approx 1000$ K, and a gas column density $N(\text{H}_2\text{O})\approx 9\times 10^{16}$ cm⁻². The density and the size are less well constrained, with values of the order a few 10^{3-4} cm⁻³ and a few arcsec, respectively.

4.2.3. Modelling consistency

Since our simple model aims at reproducing only the water line fluxes and not the line profiles, one may question its consistency with respect to the spectroscopic information of the line profiles obtained with HIFI. In other words, is there any evidence for

specific observational signatures of the two temperature components invoked in our modelling?

From Fig. 8 (top panel), it appears immediately that the bulk of flux of most of the lines in the HIFI and PACS range actually comes from the hot gas component at $T_{\text{kin}} \approx 1000$ K. Conversely, the lines at 556.9, 1669, and 1113 GHz (HIFI) are very well accounted by the warm component at $T_{\text{kin}} \approx 250$ K. This is indeed consistent with the two groups of line profiles (1113/1669 GHz and 752/998 GHz) identified (see Fig. 5 in Sect. 3.2). The line profiles are very similar within each group, and differ markedly from one group to the other. Our model provides a simple explanation to this observational fact: we are actually probing two different regions with different excitation conditions.

Second, we have compared our PACS observations with the fluxes predicted by our two-temperature model for all the water lines falling in range 50–200 μm . As can be seen in Fig. 9, most of the lines remain below the dashed line, which draws the sensitivity limit of the observations. Our model does not predict more lines lying above the sensitivity limit than those actually detected.

CO line observations with PACS and HIFI revealed a warm, dense gas component, *thermalized at 220 K*, which Benedettini et al. (2012) and Lefloch et al. (2012) attributed to the jet impact region against the B1 cavity. Both the location and the temperature of this component agree with the properties with the warm gas component identified by Nisini et al. (2010b). However, since the bulk of emission of the CO (16–15) and H₂O 1097 GHz lines arises from two components of different excitation inside the B1 cavity, we conclude that the profile of the H₂O 1097 GHz line could actually not be specific of g_1 , unlike claimed in a previous work (Lefloch et al. 2012), indicating a more complex origin of that spectral feature.

One may wonder why the CO counterpart of the second component is not detected by the sensitive PACS and HIFI instruments. This is illustrated in the bottom panel of Fig. 8, which displays the predicted CO fluxes for the hot component ($T_{\text{kin}} \approx 1000$ K, $n(\text{H}_2) = 2 \times 10^4 \text{ cm}^{-3}$, and the assumed size of $2''.5$), assuming an abundance ratio $[\text{CO}]/[\text{H}_2\text{O}] = 1$. Adopting the standard value of 10^{-4} for CO would imply a smaller value of the column density, and the flux of the hot component would be even smaller.

We point out that a similar two-component model has been presented recently by Santangelo et al. (2013) to account for the water emission towards the B2 shock position of the L1448 molecular outflow, where the physical conditions are similar to the ones obtained in L1157-B1. Confirming the presence of similar two-component structure in other shock regions would suggest that both components are most likely related to the bow-shock phenomenon itself. The nature of the relation could provide some clue onto the origin of the line profiles observed.

4.3. Cloud absorption

In Sect. 3.2, we showed that H₂O transitions connecting with the ground state level present a narrow self-absorption feature close to the ambient velocity, at $v_{\text{LSR}} \sim 2.6 \text{ km s}^{-1}$. Since optically thin lines, such as ¹³CO (Lefloch et al. in preparation) and HDO (Codella et al. 2012), peak close to the ambient velocity, we propose that the absorption feature seen in the low-excited H₂O lines most likely arises from an extended layer associated with the cloud envelope, as a result of ice photodesorption. Such a model was successfully applied recently by Coutens et al. (2012) to the low-mass Class 0 protostar IRAS 16293–2422, where the authors find a similar self-absorption signature in the fundamen-

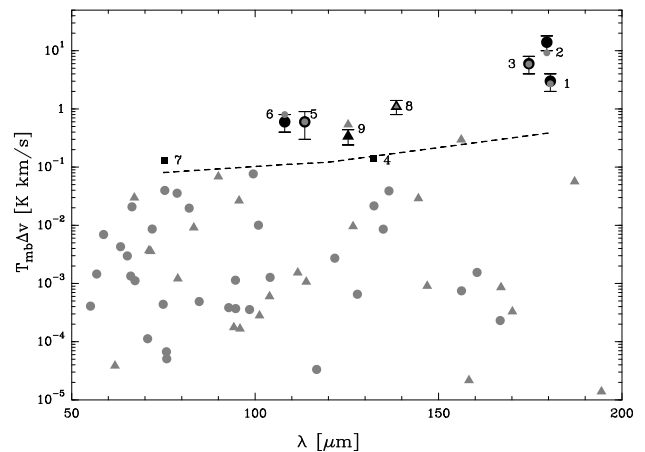


Fig. 9. Predicted H₂O fluxes in the PACS range of the two-component model, shown in Fig. 8 and Table 3, as a function of wavelength. Black/grey circles and triangles mark the observed/predicted fluxes of o-H₂O and p-H₂O lines, respectively. Squares represent upper limits of H₂O lines listed in Table 2. The line_ID is also shown (see Table 2). The dashed line indicates the sensitivity limit of PACS.

tal lines of HDO and H₂¹⁸O. In order to account for the observed line profiles, the authors added an absorbing layer in front of the IRAS 16293–2422 envelope that results from the photodesorption of icy mantles at the edge of the cloud by the FUV photons, as modeled by Hollenbach et al. (2009).

Interpreting in a similar way the absorption feature as due to a water-rich layer caused by ice photodesorption at the cloud surface, we can estimate its water abundance. Caratti o Garatti et al. (2006) evaluate the visual extinction towards the B1 shock through near-IR data and find that A_V is, at most, 2 mag. Thus, adopting A_V of 1–2 mag, assuming an incident FUV flux of $G_0 = 1$ (i.e., adopting a standard interstellar radiation field), a typical cloud gas density of 10^4 cm^{-3} , Hollenbach et al. (2009) predict a water abundance of about $\sim 10^{-7}$. At the same depth and for a fixed value of G_0 , lower densities would result in slightly lower values of the H₂O abundance. On the other hand, if we consider higher values of G_0 the water abundance, for A_V of 1–2 mag, will be lower as a higher incident flux modifies the depth of the freeze, moving it towards higher visual extinction, resulting in a peak deeper in the cloud for gas-phase H₂O. Therefore, we estimate the water abundance of the cloud absorbing layer due to the cloud $\approx 10^{-7}$. Adopting the relation $N(\text{H}_2) = 9.4 \times 10^{20} A_V$ (Frerking et al. 1982) we obtained $N(\text{H}_2) = (0.9\text{--}1.9) \times 10^{21} \text{ cm}^{-2}$ for an A_V of 1–2 mag, and hence the column density of H₂O in this absorbing layer should be about $1 \times 10^{13} \text{ cm}^{-2}$.

4.4. Water abundance and line cooling

The water abundance $X(\text{H}_2\text{O}) = [\text{H}_2\text{O}]/[\text{H}_2]$ in the shocked gas was derived using the H₂ data from Nisini et al. (2010b) obtained with *Spitzer* and convolved at the PACS resolution ($12''.7$). For the 250 K gas component, the H₂ column density was computed from an LTE analysis of the S(0) to S(2) rotational lines. For a source size of $10''$, the column density of H₂ is $N(\text{H}_2) \approx 1.2 \times 10^{20} \text{ cm}^{-2}$, which yields a fractional abundance of water $\sim (0.7\text{--}2) \times 10^{-6}$. This warm gas component is associated with a partially dissociative J-type shock either with a shock veloc-

ities and pre-shock densities of $v > 30 \text{ km s}^{-1}$ and $2 \times 10^4 \text{ cm}^{-3}$ or $v > 20 \text{ km s}^{-1}$ and $2 \times 10^5 \text{ cm}^{-3}$ (Benedettini et al. 2012; Lefloch et al. 2012), and hence the low water abundance can be explained in terms of FUV photons produced at the shock front that prevent the full conversion of free oxygen into water, resulting in a decrease of the water abundance. To obtain the water abundance of the hot gas, we considered the H_2 rotational lines S(5) up to S(7) and computed the H_2 column density scaled for a source size of size of $2''.5$. The derived water abundance is $(1.2\text{--}3.6) \times 10^{-4}$, in agreement with the predicted values for hot shocked material (Kaufman & Neufeld 1996; Bergin et al. 1998; Flower & Pineau Des Forêts 2010). The abundance of H_2O in the hot gas is two orders of magnitude higher than that obtained for the warm gas, indicating that all of the available oxygen not locked in CO has been converted to H_2O . The derived H_2O abundances are reported in Table 4.

The low water abundance associated with the warm gas component confirms previous findings in molecular outflows based on a limited number of lines (e.g., Bjerkerli et al. 2012; Vasta et al. 2012; Tafalla et al. 2013; Santangelo et al. 2013). Moreover, we also confirmed the presence of a hot gas component at higher abundance that so far has been clearly identified only for the B2 shock position of the L1448 outflow (Santangelo et al. 2013). The presence of a warm and hot water components have been suggested by Goicoechea et al. (2012) and Dionatos et al. (2013) in shocks close to several Class 0 sources in Serpens. Therefore, our results confirm that in bow-shocks far from the driving source there is a bimodal distribution, which seems to be a common shock characteristic.

Nisini et al. (2010b) obtained the line cooling due to H_2 in the B1 shock position, which is of the order of $0.03 L_\odot$ ⁵. Here, we estimated the total luminosity of water lines, $L_{\text{H}_2\text{O}}$, from the predicted line fluxes of the best-fit model shown in Fig. 8. We obtained $\sim 0.002 L_\odot$ and $\sim 0.03 L_\odot$ for the warm and the hot gas components, respectively. Regarding CO, the derived luminosity of the warm component is $0.004 L_\odot$, hence the contribution of water to the line cooling is 50 % of the CO luminosity. The luminosity of hot CO gas component, on the other hand, is $0.01 L_\odot$, and therefore the far-IR cooling of H_2O dominates in front of CO, and it contributes equally as the H_2 line cooling. The results are summarized in Table 4.

Finally, we calculated the total far-IR cooling in the B1 shock region following the definition of Nisini et al. (2002), where $L_{\text{FIR}} = L_{\text{OI}} + L_{\text{CO}} + L_{\text{H}_2\text{O}} + L_{\text{OH}}$. Using the line fluxes reported by Benedettini et al. (2012), we estimated the total luminosity of [OI] and OH, which are $L_{\text{OI}} \approx 2 \times 10^{-3} L_\odot$ and $L_{\text{OH}} \approx 4 \times 10^{-4} L_\odot$. For CO and H_2O we considered the contribution of the two gas components. One can clearly see that the far-IR cooling is dominated by the contribution of H_2O and CO lines, followed by [OI] and OH. The total far-IR cooling estimated in B1 is $\sim 0.05 L_\odot$. It is worth noticing that the FIR luminosity has been computed using similar beam sizes for all species, while the H_2 luminosity was estimated with a smaller beam.

Shock models produce markedly different predictions on the H_2O cooling function, depending on the nature of the shock, either C-type (MHD) or J-type shocks. We make here a simple comparison with the predictions from the steady-state shock models of Flower & Pineau Des Forêts (2010), for a shock propagating at $v = 20 \text{ km s}^{-1}$ into gas with pre-shock density of 10^4 cm^{-3} . Our goal is to identify qualitative trends on the properties of the shock responsible for the H_2O emission detected. As

pointed out by Gueth et al. (1996), the B1 bow-shock is propagating into gas previously accelerated by the ejection associated with B2. Maximum velocities of $5 - 10 \text{ km s}^{-1}$ are reported in the B2 outflow cavity (Vasta et al. 2012). For this reason, we consider that velocities detected in the H_2O gas towards B1 ($\approx 30 \text{ km s}^{-1}$; Fig. 4) are not inconsistent with a shock velocity of about 20 km s^{-1} .

For the warm ($T_{\text{kin}} \approx 250 \text{ K}$) gas component, the H_2O line cooling is $\approx 1.5 \times 10^{-19} \text{ erg cm}^{-3} \text{ s}^{-1}$, in agreement with the value predicted in the molecular reformation zone of a J-type shock (see Fig. 2 of Flower & Pineau Des Forêts 2010; see also Benedettini et al. 2012). For the hot ($T_{\text{kin}} \approx 1000 \text{ K}$) gas component, the H_2O line cooling is $\approx 2 \times 10^{-16} \text{ erg cm}^{-3} \text{ s}^{-1}$, a value several order of magnitude higher than that predicted by the C-shock model, but well in the range of values expected in the J-type shock. Therefore, the simple comparison suggests that the hot gas layer is excited in a non-dissociative J-type shock.

5. Summary and Conclusions

As part of the CHESs key program, we have analyzed the H_2O emission towards the shock region L1157-B1. A grand total of 13 H_2O lines (both ortho and para) have been detected with HIFI and PACS instruments arising from transitions with rather low E_u , from 26.7 K to 319.5 K. The PACS and HIFI observations towards the L1157-B1 bow-shock have revealed the presence of several gas components with different excitation. Our main conclusions can be summarized as follows :

1. The bulk of H_2O emission originates in the B1 bow-shock.
2. An absorption feature is detected in the line profiles connecting with the ground state level. It arises from a water-enriched layer ($X[\text{H}_2\text{O}] \approx 10^{-7}$) at the surface of the cloud formed as a result of water ice photodesorption from interstellar grain mantles, driven by the external UV photons due to the interstellar radiation field.
3. The LVG analysis of the H_2O emission associated with the bright high-excitation region (i.e., the bow-shock) has permitted us to identify two physical components. A warm, dense gas ($T_{\text{kin}} \sim 200\text{--}300 \text{ K}$, $n(\text{H}_2) \approx (1\text{--}3) \times 10^6 \text{ cm}^{-3}$) component traced mainly by the low-excitation lines of water (shown in blue in Fig. 7), with an assumed extent of $10''$. The OPR- H_2 in the warm gas is ≈ 0.5 . The hot ($T_{\text{kin}} \approx 1000 \text{ K}$) component is made of tenuous gas at a much lower density (a few $10^{3\text{--}4} \text{ cm}^{-3}$) similar to that of the parental cloud. It is much more compact, with a typical size of $2'' - 5''$. The OPR- H_2 in the warm gas is ≈ 3.0 , equal to its value at LTE.
4. These two shock components present marked differences in terms of water enrichment. While the derived abundance in the warm gas is $(0.7\text{--}2) \times 10^{-6}$, the water abundance estimated in the hot gas is much higher, around $(1.2\text{--}3.6) \times 10^{-4}$, indicating that all available oxygen not locked in CO is driven into H_2O . The FIR cooling of the bow-shock appears to be equally dominated by both H_2 and the hot water component.
5. A simple comparison of the water line cooling properties with the steady-state shock models of Flower & Pineau Des Forêts (2010) is consistent with a J-type shock origin for both components. The exact nature of the hot water spot and its relation with the jet impact against the cavity remains to be established. The low density of the hot H_2O gas suggests that the shock propagates into a region of much lower density, either in the ambient cloud or the outflow cavity gas.

⁵ L_{H_2} has been corrected for a distance of 250 pc while in Nisini et al. (2010b) the adopted distance is 440 pc.

Higher-angular observations are needed to understand the structure of the L1157-B1 bow-shock region. We expect that a detailed, multiline study and comparison of the emission properties of the major cooling agents, CO, H₂O and H₂ at infrared wavelengths with shock model predictions, will help us to clarify the origin and the relation the different shock components revealed by PACS and HIFI hold to each other (Cabrit et al. in preparation).

Acknowledgements. The authors are grateful to the anonymous referee and the Editor Dr. Malcolm Walmsley for valuable comments. G.B is grateful to M. Pereira-Santaella for fruitful discussion. G. Busquet, M. Benedettini, C. Codella, B. Nisini, A. I. Gómez-Ruiz, and A. M. di Giorgio are supported by the Italian Space Agency (ASI) project I/005/11/0. B. Lefloch thanks the Spanish MEC for funding support through grant SAB2009-0011. B. Lefloch, C. Ceccarelli, and L. Wiesenfeld acknowledge funding from the French Space Agency CNES and the National Research Agency funded project FORCOM, ANR-08-BLAN-0225. S. Viti acknowledges support from the [European Community's] Seventh Framework Programme [FP7/2007-2013] under grant agreement n° 238258. A. Gusdorf acknowledges support by the grant ANR-09-BLAN-0231-01 from the French Agence Nationale de la Recherche as part of the SCHISM project. HIFI has been designed and built by a consortium of institutes and university departments from across Europe, Canada and the United States under the leadership of SRON Netherlands Institute for Space Research, Groningen, The Netherlands and with major contributions from Germany, France and the US. Consortium members are: Canada: CSA, UWaterloo; France: CESR, LAB, LERMA, IRAM; Germany: KOSMA, MPIfR, MPS; Ireland, NUI Maynooth; Italy: ASI, IFSI-INAF, Osservatorio Astrofisico di Arcetri-INAF; Netherlands: SRON, TUD; Poland: CAMK, CBK; Spain: Observatorio Astronómico Nacional (IGN), Centro de Astrobiología (CSIC-INTA). Sweden: Chalmers University of Technology - MC2, RSS & GARD; Onsala Space Observatory; Swedish National Space Board, Stockholm University - Stockholm Observatory; Switzerland: ETH Zurich, FHNW; USA: Caltech, JPL, NHSC. PACS has been developed by a consortium of institutes led by MPE (Germany) and including UVIE (Austria); KU Leuven, CSL, IMEC (Belgium); CEA, LAM (France); MPIA (Germany); INAF-IFSI/OAA/OAP/OAT, LENS, SISSA (Italy); IAC (Spain). This development has been supported by the funding agencies BMVIT (Austria), ESA-PRODEX (Belgium), CEA/CNES (France), DLR (Germany), ASI/INAF (Italy), and CICYT/MCYT (Spain).

References

- Arce, H. G., Santiago-García, J., Jørgensen, J. K., Tafalla, M., & Bachiller, R. 2008, *ApJ*, 681, L21
- Bachiller, R. 1996, *ARA&A*, 34, 111
- Bachiller, R. & Perez Gutierrez, M. 1997, *ApJ*, 487, L93
- Bachiller, R., Pérez Gutiérrez, M., Kumar, M. S. N., & Tafalla, M. 2001, *A&A*, 372, 899
- Benedettini, M., Busquet, G., Lefloch, B., et al. 2012, *A&A*, 539, L3
- Benedettini, M., Viti, S., Codella, C., et al. 2007, *MNRAS*, 381, 1127
- Benedettini, M., Viti, S., Codella, C., et al. 2013, *MNRAS*, 436, 179
- Bergin, E. A., Neufeld, D. A., & Melnick, G. J. 1998, *ApJ*, 499, 777
- Bjerkeli, P., Liseau, R., Larsson, B., et al. 2012, *A&A*, 546, A29
- Bjerkeli, P., Liseau, R., Nisini, B., et al. 2013, *A&A*, 552, L8
- Bjerkeli, P., Liseau, R., Olberg, M., et al. 2009, *A&A*, 507, 1455
- Caratti o Garatti, A., Giannini, T., Nisini, B., & Lorenzetti, D. 2006, *A&A*, 449, 1077
- Ceccarelli, C., Bacmann, A., Boogert, A., et al. 2010, *A&A*, 521, L22
- Ceccarelli, C., Maret, S., Tielens, A. G. G. M., Castets, A., & Caux, E. 2003, *A&A*, 410, 587
- Codella, C., Benedettini, M., Beltrán, M. T., et al. 2009, *A&A*, 507, L25
- Codella, C., Ceccarelli, C., Lefloch, B., et al. 2012, *ApJ*, 757, L9
- Codella, C., Lefloch, B., Ceccarelli, C., et al. 2010, *A&A*, 518, L112
- Coutens, A., Vastel, C., Caux, E., et al. 2012, *A&A*, 539, A132
- Daniel, F., Dubernet, M.-L., & Grosjean, A. 2011, *A&A*, 536, A76
- Daniel, F., Dubernet, M.-L., Pacaud, F., & Grosjean, A. 2010, *A&A*, 517, A13
- Davis, C. J. & Eisloffel, J. 1995, *A&A*, 300, 851
- de Graauw, T., Helmich, F. P., Phillips, T. G., et al. 2010, *A&A*, 518, L6
- Dionatos, O., Jørgensen, J. K., Green, J. D., et al. 2013, *ArXiv e-prints*
- Draine, B. T., Roberge, W. G., & Dalgarno, A. 1983, *ApJ*, 264, 485
- Dubernet, M.-L., Alexander, M. H., Ba, Y. A., et al. 2013, *A&A*, 553, A50
- Dubernet, M.-L., Daniel, F., Grosjean, A., & Lin, C. Y. 2009, *A&A*, 497, 911
- Dubernet, M.-L., Grosjean, A., Flower, D., et al. 2006, *Journal of Plasma Research SERIES*, Volume 7, p. 356-357, 7, 356
- Flower, D. R. & Pineau Des Forêts, G. 2010, *MNRAS*, 406, 1745
- Flower, D. R. & Pineau des Forêts, G. 2012, *MNRAS*, 421, 2786
- Franklin, J., Snell, R. L., Kaufman, M. J., et al. 2008, *ApJ*, 674, 1015
- Frerking, M. A., Langer, W. D., & Wilson, R. W. 1982, *ApJ*, 262, 590
- Giannini, T., Nisini, B., & Lorenzetti, D. 2001, *ApJ*, 555, 40
- Goicoechea, J. R., Cernicharo, J., Karska, A., et al. 2012, *A&A*, 548, A77
- Gueth, F., Guilloteau, S., & Bachiller, R. 1996, *A&A*, 307, 891
- Gueth, F., Guilloteau, S., & Bachiller, R. 1998, *A&A*, 333, 287
- Gusdorf, A., Cabrit, S., Flower, D. R., & Pineau Des Forêts, G. 2008a, *A&A*, 482, 809
- Gusdorf, A., Pineau Des Forêts, G., Cabrit, S., & Flower, D. R. 2008b, *A&A*, 490, 695
- Hollenbach, D., Kaufman, M. J., Bergin, E. A., & Melnick, G. J. 2009, *ApJ*, 690, 1497
- Hollenbach, D. & McKee, C. F. 1989, *ApJ*, 342, 306
- Kaufman, M. J. & Neufeld, D. A. 1996, *ApJ*, 456, 611
- Lefloch, B., Cabrit, S., Busquet, G., et al. 2012, *ApJ*, 757, L25
- Lefloch, B., Cernicharo, J., Cabrit, S., et al. 2003, *ApJ*, 590, L41
- Looney, L. W., Tobin, J. J., & Kwon, W. 2007, *ApJ*, 670, L131
- Maret, S., Bergin, E. A., Neufeld, D. A., et al. 2009, *ApJ*, 698, 1244
- Neufeld, D. A., Melnick, G. J., & Harwit, M. 1998, *ApJ*, 506, L75
- Neufeld, D. A., Melnick, G. J., Sonnentrucker, P., et al. 2006, *ApJ*, 649, 816
- Neufeld, D. A., Nisini, B., Giannini, T., et al. 2009, *ApJ*, 706, 170
- Nisini, B., Benedettini, M., Codella, C., et al. 2010a, *A&A*, 518, L120
- Nisini, B., Codella, C., Giannini, T., et al. 2007, *A&A*, 462, 163
- Nisini, B., Giannini, T., & Lorenzetti, D. 2002, *ApJ*, 574, 246
- Nisini, B., Giannini, T., Neufeld, D. A., et al. 2010b, *ApJ*, 724, 69
- Ott, S. 2010, in *Astronomical Society of the Pacific Conference Series*, Vol. 434, *Astronomical Data Analysis Software and Systems XIX*, ed. Y. Mizumoto, K.-I. Morita, & M. Ohishi, 139
- Pickett, H. M., Poynter, R. L., Cohen, E. A., et al. 1998, *J. Quant. Spec. Radiat. Transf.*, 60, 883
- Pilbratt, G. L., Riedinger, J. R., Passvogel, T., et al. 2010, *A&A*, 518, L1
- Poglitsch, A., Waelkens, C., Geis, N., et al. 2010, *A&A*, 518, L2
- Roelfsema, P. R., Helmich, F. P., Teysseier, D., et al. 2012, *A&A*, 537, A17
- Santangelo, G., Nisini, B., Antonucci, S., et al. 2013, *A&A*, 557, A22
- Tafalla, M. & Bachiller, R. 1995, *ApJ*, 443, L37
- Tafalla, M., Liseau, R., Nisini, B., et al. 2013, *A&A*, 551, A116
- Takami, M., Karr, J. L., Nisini, B., & Ray, T. P. 2011, *ApJ*, 743, 193
- van Dishoeck, E. F., Kristensen, L. E., Benz, A. O., et al. 2011, *PASP*, 123, 138
- Vasta, M., Codella, C., Lorenzani, A., et al. 2012, *A&A*, 537, A98
- Wilgenbus, D., Cabrit, S., Pineau des Forêts, G., & Flower, D. R. 2000, *A&A*, 356, 1010
- Zhang, Q., Ho, P. T. P., & Wright, M. C. H. 2000, *AJ*, 119, 1345